ELSEVIER

Comput. Methods Appl. Mech. Engrg. 190 (2001) 3271–3292

Computer methods in applied mechanics and engineering

www.elsevier.com/locate/cma

A meshfree contact-detection algorithm

Shaofan Li, Dong Qian, Wing Kam Liu *, Ted Belytschko

Department of Mechanical Engineering, The Technological Institute, Northwestern University, 2145 Sheridan Road, Evanston, IL 60208, USA

Received 7 September 1999

Abstract

A new contact-detection algorithm is proposed, which is based on the moment matrix of the meshfree interpolation. This new contact-detection algorithm has several advantages over conventional contact-detection algorithms; they are ease of implementation, accuracy in detection. It is scalable in parallel computations, and applicable to a wide variety of problems. Because the moment matrix is computed in constructing meshfree approximation, the algorithm is very suitable for meshfree computations, though it can be used in finite element computations as well. Moreover, such contact-detection algorithm can be conveniently implemented to detect self-contact. Both algorithmic and mathematical aspects of the contact algorithm are discussed in the paper. To validate the proposed contact algorithm, the Taylor bar problem is computed using both meshfree method and finite element method (FEM) to simulate a viscoplastic projectile impacting with a rigid target at high speed. Numerical results obtained with the meshfree contact algorithm show that this new contact algorithm can accurately predict the contact as well as separation of projectile and target. In addition, the numerical results obtained show distinct and detailed shear band formations occurring in the impact event.

Keywords: Contact–impact; Finite element methods; Meshfree methods; Shear band formation; Scalable parallel computing; Viscoplasticity

1. Introduction

The numerical simulation of contact between two different objects, or different parts of an object is a serious challenge in many engineering applications such as sheet metal forming, vehicle crash-worthiness, impact, penetration and fragmentation, large deformation of shell-type structures, and machining in manufactures, etc. In some situations, for instance, the large deformation of thin shell structures, a so-called self-contact phenomenon may also occur, which is very difficult to model in numerical simulations because of the complex nature of the problem. If the computation is performed without considering self-contact; unrealistic inter-penetration of different parts of the shell can be observed in the numerical computation. Fig. 1 shows such an example – a deformed cylindrical shell under axial compression.

There have been several contact-detection algorithms proposed in literature, such as *Benson–Hallquist* algorithm proposed by Benson & Hallquist [10,14], *Pinball* algorithm proposed by Belytschko et al. [7,8], *Point-in-box* search algorithm by Heinstein et al. [15], and the recent *bounding box* algorithms by Malone & Johnson [28,29] and Attaway et al. [3], which are designated for parallel computation. Most of the these algorithms are complicated in implementation, especially in parallel computations, because they are

* Corresponding author. Tel.: +1-847-491-7094; fax: +1-847-491-3915.

E-mail addresses: sf-li@nwu.edu (S. Li), d-qian@nwu.edu (D. Qian), w-liu@nwu.edu (W. Kam Liu), t-belytschko@nwu.edu (T. Belytschko).

0045-7825/01/$ - see front matter
PII: S0045-7825(00)00392-3

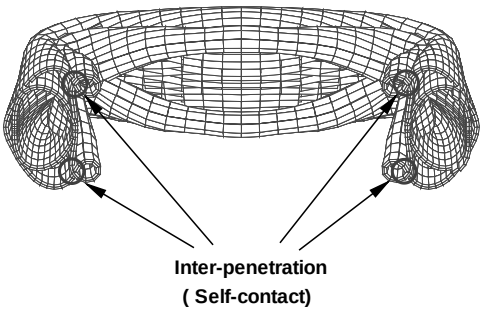

Fig. 1. Computation failure due to self-contact: a cylindrical shell subjected to axial compression.

involved with multiple vector operations and multiple conditional statements even for a single surface check, or single bounding box check.

Recently, a new generation of numerical methods called "meshfree" methods has emerged, and it has a profound impact on computational mechanics. Three special issues of research papers have been devoted to the subject: the special issue in Computer Methods in Applied Mechanics and Engineering (Vol. 139, 1996) Edited by Liu, Belytschko and Oden, the special issue in Int. J. Numer. Methods Engrg. (Vol. 49 No. 5, 2000) edited by Liu, Idelsohn and Onate; and the special issue in Comput. Mech. (Vol. 2/3, 2000) edited by Chen and Liu. In many meshfree methods, the construction of the approximation requires moment matrix; these include the element-free Galerkin (EFG) method by Belytschko et al. [5,6], the reproducing kernel particle method (RKPM) by Liu et al. [20–27], *h-p* Cloud method by Duarte and Oden [12,13], and the meshfree local Petrov–Galerkin (MLPG) method by Atluri and Zhu [1,2].

It has been found that this moment matrix provides a natural indicator to track the surface, or interface of any continuum object. In this paper, we address the fundamental issue of contact algorithm, i.e., contact-detection problem. This problem is deeply rooted in the question on how to accurately represent a geometric object with simple rules, and to detect the contact region by simple criterion. Based on the principle of moment of meshfree interpolation, a new contact-detection algorithm is proposed. Most remarkably, the proposed meshfree contact-detection criterion is a scalar criterion, which is easy to implement, and accurate.

The presentation is organized as follows. In Section 2, the meshfree contact-detection algorithm – a moment method is presented. In Section 3, the mathematical principle of meshfree representation of a geometric object is discussed. A brief outline of constitutive model, time integration and discretization is given in Section 4. The impenetrability and frictional conditions at the contact interface are dealt with in Section 5. Numerical results obtained by the proposed meshfree contact algorithm are reported in Section 6.

2. The meshfree contact-detection algorithm: a moment method

Before describing the meshfree contact-detection algorithm, it is expedient to recapitulate the basic procedure on how to construct moment matrix in one of the meshfree methods – reproducing kernel particle method [26,27]. Assume that the window function is given such that for fixed $\mathbf{x} \in \mathbb{R}^n$,

$$\phi_\rho(\mathbf{y}-\mathbf{x}) = \begin{cases} > 0, & \mathbf{y} \in \operatorname{supp}\{\phi_\rho(\mathbf{y}-\mathbf{x})\}, \\ = 0, & \mathbf{y} \notin \operatorname{supp}\{\phi_\rho(\mathbf{y}-\mathbf{x})\}, \end{cases} \tag{1}$$

where ρ is the dilation parameter, which is the characteristic length of the support size, and in this paper it is sometimes referred to as the radius of the compact support in a way of speaking. [1] And

[1] If the compact support is a circle, in 2D for instance, ρ is the radius of the compact support; if the shape of the support is a rectangle, the radius of a compact support is not well defined.

$$\phi_\rho(\mathbf{x}) := \frac{1}{\rho^n}\phi\left(\frac{\mathbf{x}}{\rho}\right). \tag{2}$$

And a polynomial basis is given as

$$\mathbf{P}(\mathbf{x}) := \{P_1(\mathbf{x}), P_2(\mathbf{x}), P_3(\mathbf{x}), \ldots, P_m(\mathbf{x})\}, \tag{3}$$

where $P_i(\mathbf{x})$ are monomial functions in ascending order, usually $P_1(\mathbf{x}) = 1$. The so-called meshfree discretization is a particle distribution, we always assume that there are NP numbers of particles residing in the domain of interest, $\bar{\Omega}$. For each particle in the domain, there is a window function associated with it, i.e.,

$$\phi_{\rho I}(\mathbf{x}) := \phi_\rho(\mathbf{x}_I - \mathbf{x}). \tag{4}$$

The moment matrix is defined as

$$\mathbf{M}^h(\mathbf{x}) = \sum_{\ell\in\Lambda} \mathbf{P}^{\mathrm{T}}\left(\frac{\mathbf{x}_\ell - \mathbf{x}}{\rho}\right)\phi_\rho(\mathbf{x}_\ell - \mathbf{x})\mathbf{P}\left(\frac{\mathbf{x}_\ell - \mathbf{x}}{\rho}\right)\Delta V_\ell \tag{5}$$

or in component form

$$M^h_{ij} = \sum_{\ell\in\Lambda} P_i\left(\frac{\mathbf{x}_\ell - \mathbf{x}}{\rho}\right)\phi_\rho(\mathbf{x}_\ell - \mathbf{x})P_j\left(\frac{\mathbf{x}_\ell - \mathbf{x}}{\rho}\right)\Delta V_\ell, \tag{6}$$

where $\Lambda := \{\ell \,|\, 1, 2, \ldots, \mathrm{NP}\}$ is the particle index set. In one-dimensional case, we often choose the polynomial basis as $\mathbf{P}(x) = (1, x, x^2, x^3, \ldots, x^{m-1})$. Hence, the components of the moment matrix, M_{ij}, is

$$\begin{aligned} M_{ij}(x) &= \sum_{\ell\in\Lambda}\left(\frac{x_\ell - x}{\rho}\right)^{i+j-2}\phi_\rho(x_\ell - x)\Delta x_\ell \\ &= \sum_{\ell\in\Lambda} z_\ell^{i+j-2}\phi(z_\ell)\Delta z_\ell, \quad \Leftarrow\ z_\ell := (x_\ell - x)/\rho \end{aligned} \tag{7}$$

which is exactly the discrete moment defined in elementary mechanics.

Example 2.1. Consider a line segment, $[0, 1]$, in one-dimensional case. We choose the cubic spline function

$$\phi(x) = \begin{cases} \frac{1}{6}(2+x)^3, & -2 \leqslant x < -1, \\ \frac{2}{3} - x^2\left(1 + \frac{x}{2}\right), & -1 \leqslant x < 0, \\ \frac{2}{3} - x^2\left(1 - \frac{x}{2}\right), & 0 \leqslant x < 1, \\ \frac{1}{6}(2-x)^3, & 1 \leqslant x < 2 \end{cases} \tag{8}$$

as the window function. There are $\mathrm{NP} = 41$ particles evenly distributed in the segment $[0, 1]$. Let $\rho = 2.0\,\Delta x$ and choose a polynomial basis as $\mathbf{P}(x) = (1, x)$. The moment matrix is then obtained as

$$\mathbf{M}^h(x) = \begin{pmatrix} m^h_{11} & m^h_{12} \\ m^h_{21} & m^h_{22} \end{pmatrix}, \tag{9}$$

where

$$m^h_{11}(x) = \sum_{\ell\in\Lambda}\phi_\rho(x_\ell - x)\Delta x_\ell, \tag{10}$$

$$m^h_{12}(x) = m^h_{21} = \sum_{\ell\in\Lambda}\left(\frac{x_\ell - x}{\rho}\right)\phi_\rho(x_\ell - x)\Delta x_\ell, \tag{11}$$

$$m_{22}^h(x) = \sum_{\ell \in \Lambda} \left(\frac{x_\ell - x}{\rho} \right)^2 \phi_\rho(x_\ell - x) \Delta x_\ell, \tag{12}$$

In Figs. 2 and 3, we plot the determinant of the moment matrix in the region, $[-0.5, 1.5]$. Inside the domain of meshfree discretization, the determinant of the moment matrix has a finite positive value, and outside $[0, 1]$, $\det\{\mathbf{M}(x)\} \to 0$.

Example 2.2. Consider a 2D example. The window function is chosen as a 2D cubic spline box, i.e., the Cartesian product, $\phi(x, y) = \phi(x)\phi(y)$. A bilinear polynomial basis, $\mathbf{P}(\mathbf{x}) = (1, x, y, xy)$, is used in construction of moment matrix, which is

$$\mathbf{M}^h(\mathbf{x}) = \begin{pmatrix} m_{11}^h & m_{12}^h & m_{13}^h & m_{14}^h \\ m_{21}^h & m_{22}^h & m_{23}^h & m_{24}^h \\ m_{31}^h & m_{32}^h & m_{33}^h & m_{34}^h \\ m_{41}^h & m_{42}^h & m_{43}^h & m_{44}^h \end{pmatrix}, \tag{13}$$

where

$$m_{11}^h(\mathbf{x}) = \sum_{\ell \in \Lambda} \phi_\rho(\mathbf{x}_\ell - \mathbf{x}) \Delta V_\ell, \tag{14}$$

$$m_{12}^h(\mathbf{x}) = \sum_{\ell \in \Lambda} \left(\frac{x_\ell - x}{\rho_x} \right) \phi_\rho(\mathbf{x}_\ell - \mathbf{x}) \Delta V_\ell, \tag{15}$$

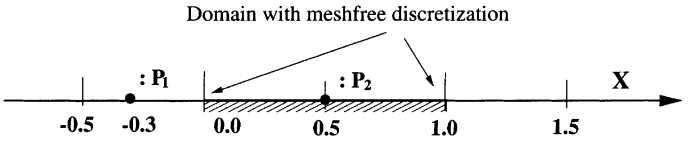

Fig. 2. A one-dimensional example: the discretized domain: $[0.0, 1.0]$ the total computed region $[-0.5, 1.5]$, and the marked points: $P_1 = -0.3$; $P_2 = 0.5$.

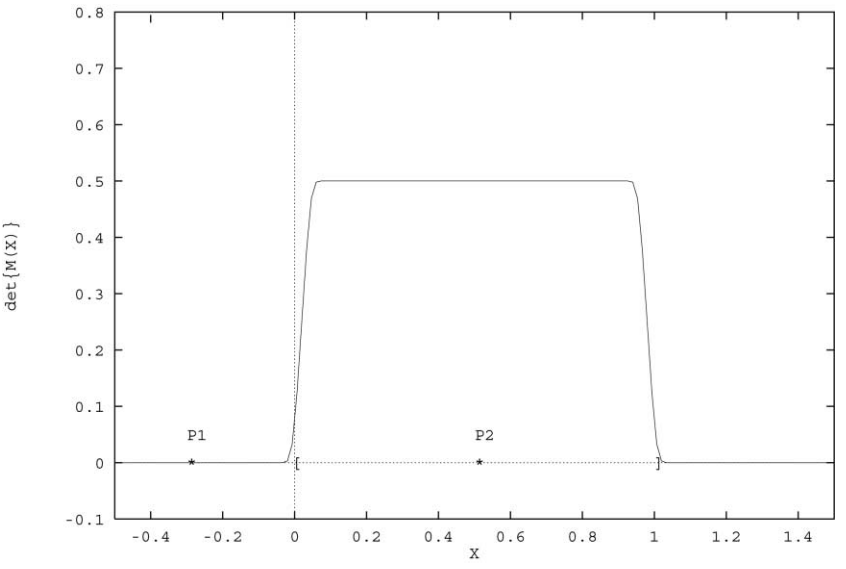

Fig. 3. The profile of the determinant of a moment matrix in one dimension.

$$m_{13}^h(\mathbf{x}) = \sum_{\ell\in\Lambda}\left(\frac{y_\ell - y}{\rho_y}\right)\phi_\rho(\mathbf{x}_\ell - \mathbf{x})\Delta V_\ell, \tag{16}$$

$$m_{14}^h(\mathbf{x}) = \sum_{\ell\in\Lambda}\left(\frac{x_\ell - x}{\rho_x}\right)\left(\frac{y_\ell - y}{\rho_y}\right)\phi_\rho(\mathbf{x}_\ell - \mathbf{x})\Delta V_\ell, \tag{17}$$

$$m_{22}^h(\mathbf{x}) = \sum_{\ell\in\Lambda}\left(\frac{x_\ell - x}{\rho_x}\right)^2\phi_\rho(\mathbf{x}_\ell - \mathbf{x})\Delta V_\ell, \tag{18}$$

$$m_{23}^h(\mathbf{x}) = m_{14}^h(\mathbf{x}), \tag{19}$$

$$m_{24}^h(\mathbf{x}) = \sum_{\ell\in\Lambda}\left(\frac{x_\ell - x}{\rho_x}\right)^2\left(\frac{y_\ell - y}{\rho_y}\right)\phi_\rho(\mathbf{x}_\ell - \mathbf{x})\Delta V_\ell, \tag{20}$$

$$m_{33}^h(\mathbf{x}) = \sum_{\ell\in\Lambda}\left(\frac{y_\ell - y}{\rho_y}\right)^2\phi_\rho(\mathbf{x}_\ell - \mathbf{x})\Delta V_\ell, \tag{21}$$

$$m_{34}^h(\mathbf{x}) = \sum_{\ell\in\Lambda}\left(\frac{x_\ell - x}{\rho_x}\right)\left(\frac{y_\ell - y}{\rho_y}\right)^2\phi_\rho(\mathbf{x}_\ell - \mathbf{x})\Delta V_\ell, \tag{22}$$

$$m_{44}^h(\mathbf{x}) = \sum_{\ell\in\Lambda}\left(\frac{x_\ell - x}{\rho_x}\right)^2\left(\frac{y_\ell - y}{\rho_y}\right)^2\phi_\rho(\mathbf{x}_\ell - \mathbf{x})\Delta V_\ell, \tag{23}$$

where $\Delta V_\ell := \Delta x_\ell \Delta y_\ell$, $\rho_x = 2.0\Delta x$, and $\rho_y = 2.0\Delta y$. Note that the moment matrix is a Gram matrix, and $M_{ij} = M_{ji}$. A total number, $\mathrm{NP} = 41 \times 21 = 861$, of particles are distributed uniformly in the domain, $[5, 25] \times [5, 15]$ (see Fig. 4). The determinant of the moment matrix is plotted in the region $[0, 20] \times [0, 30]$ as shown in Fig. 5. Once again, inside the discretized domain $\det\{\mathbf{M}(\mathbf{x})\}$ has a finite, positive value; and outside this domain $\det\{\mathbf{M}(\mathbf{x})\} \to 0$.

We tested the same window function and polynomial basis in a 2D concave domain (Fig. 6). A total 265 particles are used in the discretization. The value of $\det\{\mathbf{M}(\mathbf{x})\}$ is plotted as the height of z-axis on the x–y

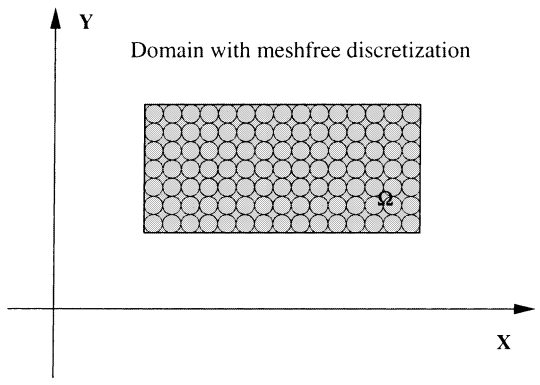

Fig. 4. Example 2.2: a meshfree discretization in a convex region.

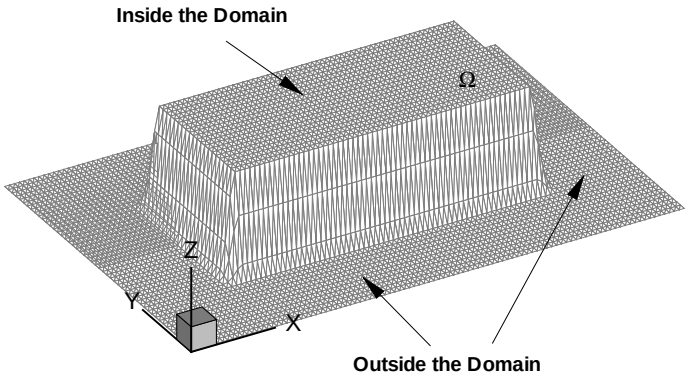

Fig. 5. The profiles of the determinant of the moment matrix in a convex region (the value of $\det\{\mathbf{M}(\mathbf{x})\}$ is plotted along the z-axis).

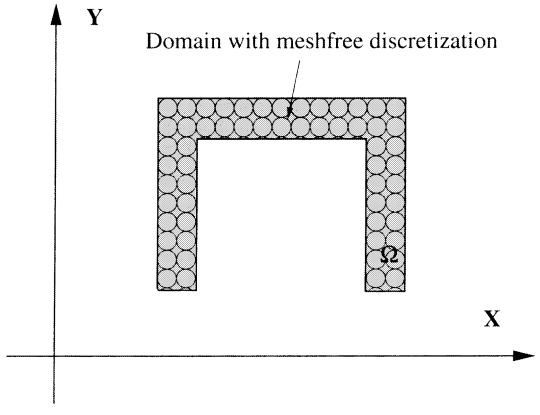

Fig. 6. A meshfree discretization in a concave region.

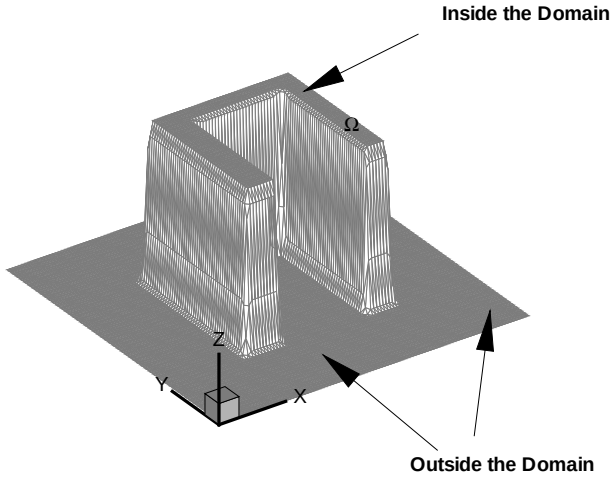

Fig. 7. The profiles of the determinant of the moment matrix in a concave region (the value of $\det\{\mathbf{M}(\mathbf{x})\}$ is plotted along the z-axis).

plane. From Fig. 7, one finds that inside the concave domain, $\det\{\mathbf{M}(\mathbf{x})\}$ has a positive value, and outside $\bar{\Omega}$, $\det\{\mathbf{M}(\mathbf{x})\} \to 0$.

One may notice that between $\bar{\Omega}$ and the region that $\{\mathbf{x} | \det\{\mathbf{M}(\mathbf{x})\} = 0\}$ there is a small buffer zone, i.e., the transition is not a clear cut. Since $\det\{\mathbf{M}(\mathbf{x})\}$ is a continuous function in space, there is ramp over the

buffer zone; i.e., the determinant of the moment matrix is not immediately becoming 0 after $\mathbf{x}$ leaving Ω, though its value in the buffer zone is a small positive number. The closer a point, $\mathbf{x}$, to Ω, the bigger value $\det\{\mathbf{M}(\mathbf{x})\}$ attains. Nevertheless, the point in the buffer zone and the point inside the domain can be still discriminated by setting a small threshold value, or tolerance, say ϵ_{cr}.

To summarized the above examples, we have the following proposition.

Proposition 2.1. *For a given domain $\Omega \in \mathbb{R}^n$ that has admissible meshfree discretization, if a spatial point, $\mathbf{x} \notin \Omega$, is sufficiently away from Ω, the determinant of the moment matrix at point, $\mathbf{x} : (x_1, x_2, x_3)$, will approach to 0; i.e., for given $\delta > 0$ $\exists \epsilon \geqslant 0$, such that if* $\mathrm{dist}\{\bar{\Omega}, \mathbf{x}\} > \delta$

$$\det\{\mathbf{M}(\mathbf{x})\} < \epsilon, \quad \mathbf{x} = (x_1, x_2, x_3). \tag{24}$$

In essence, the proposition can be interpreted as: if a continuum is discretized by a moment-based meshfree method, one can distinguish the inside of continuum from the domain's external by checking the determinant of the moment matrix. The usefulness of the above property is that one can accurately track the spatial position of any continuum in a deformation process without knowing the exact shape of its boundary, which, in general, is almost impossible to know anyway. This property provides us a numerical means to track the evolution of an interface, as well as the movement of a spatial object in a Lagrangian manner.

Now we are in a position to discuss the meshfree contact algorithm. To illustrate the contact algorithm, we consider a simple Taylor bar impact problem, i.e., a deformable solid bar impacts with rigid target as shown in Fig. 8(a).

Fig. 8(b) shows two admissible particle distributions in rigid target (master body) and in deformable Taylor bar (slave body), respectively. In computations, both objects are discretized by meshfree particle distributions, and each particle distribution has its own moment matrix, $\mathbf{M}_{\mathrm{m}}(\mathbf{x})$ and $\mathbf{M}_{\mathrm{s}}(\mathbf{x})$, and their

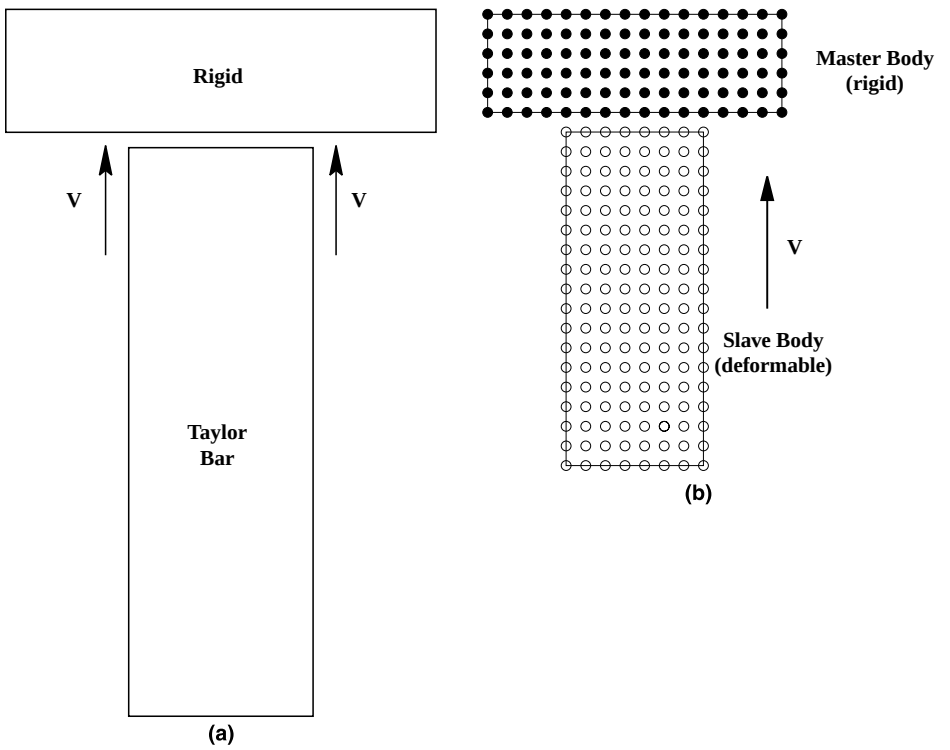

Fig. 8. The Taylor bar problem: (a) problem statement; (b) admissible particle discretizations.

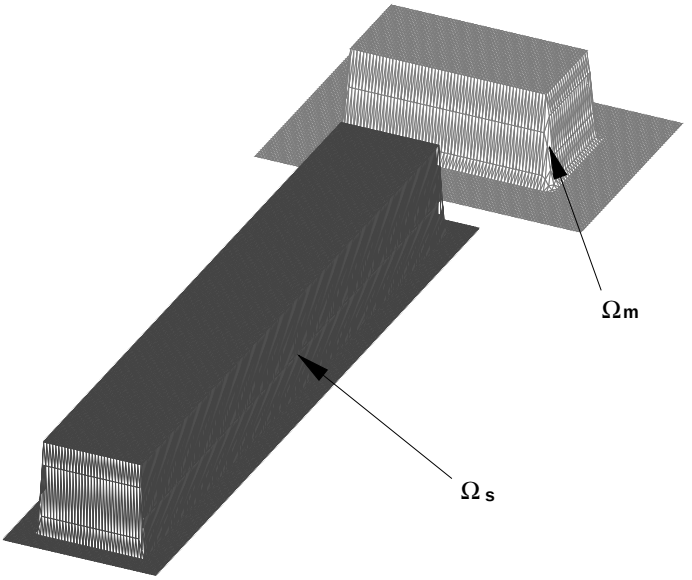

Fig. 9. The profiles of determinant of moment matrixs in projectile and target.

determinants, $\det\{\mathbf{M}_{\mathrm{m}}(\mathbf{x})\}$ and $\det\{\mathbf{M}_{\mathrm{s}}(\mathbf{x})\}$ respectively. In Fig. 9, both $\det\{\mathbf{M}_{\mathrm{m}}(\mathbf{x})\}$ and $\det\{\mathbf{M}_{\mathrm{s}}(\mathbf{x})\}$ are plotted along z-axis.

If there is no overlap or interpenetration between the two objects, for any spatial point in space, only one of the determinants will be positive, i.e., for fixed $\mathbf{x} \in \mathbb{R}^n$

$$\det\{\mathbf{M}_{\mathrm{m}}(\mathbf{x})\} > 0, \quad \det\{\mathbf{M}_{\mathrm{s}}(\mathbf{x})\} = 0, \tag{25}$$

or

$$\det\{\mathbf{M}_{\mathrm{m}}(\mathbf{x})\} = 0, \quad \det\{\mathbf{M}_{\mathrm{s}}(\mathbf{x})\} > 0. \tag{26}$$

More precisely, if there is no inter-penetration, one will find that

$$\boxed{\begin{array}{l} \text{1. No penetration : } (\Omega_{\mathrm{m}} \cap \Omega_{\mathrm{s}} = \emptyset) \\ \mathbf{M}_{\mathrm{m}}(\mathbf{x}) \to 0 \quad \forall \mathbf{x} \in \Omega_{\mathrm{s}} \\ \mathbf{M}_{\mathrm{s}}(\mathbf{x}) \to 0 \quad \forall \mathbf{x} \in \Omega_{\mathrm{m}} \end{array}} \tag{27}$$

Otherwise, if there is penetration in certain area, for given tolerance $\epsilon_{\mathrm{cr}} > 0$

$$\boxed{\begin{array}{l} \text{2. Inter-penetration : } (\Omega_{\mathrm{m}} \cap \Omega_{\mathrm{s}} \neq \emptyset) \\ \mathbf{M}_{\mathrm{m}}(\mathbf{x}) > \epsilon_{\mathrm{cr}}, \quad \text{for some } \mathbf{x} \in \Omega_{\mathrm{s}} \\ \mathbf{M}_{\mathrm{s}}(\mathbf{x}) > \epsilon_{\mathrm{cr}}, \quad \text{for some } \mathbf{x} \in \Omega_{\mathrm{m}} \end{array}} \tag{28}$$

In the Taylor problem, since the target is a rigid body, which has no movement, we only need to check the first part of contact/penetration condition in (27) or (28). Fig. 8(b) shows two admissible particle distributions: one in rigid target (master body) and the other in deformable Taylor bar (slave body).

By computing the determinant of the moment matrix in master domain for both master body and slave body (slave body is a moving object in the case), inter-penetration of the two bodies can be easily detected. Fig. 10(a) shows that before the Taylor bar makes contact with the rigid target: for all the particles in slave body, $\mathbf{x} \in \bar{\Omega}_{\mathrm{s}}$, $\det\{\mathbf{M}_{\mathrm{s}}(\mathbf{x})\} \to 0$, which is represented by a dark region with zero value in z coordinate. The non-zero plateau in Fig. 10(a) represents the fact that $\forall \mathbf{x} \in \bar{\Omega}_{\mathrm{m}}$, $\det\{\mathbf{M}_{\mathrm{m}}(\mathbf{x})\}$ is a finite positive number, or $\det\{\mathbf{M}_{\mathrm{m}}(\mathbf{x})\} \geqslant \epsilon_{\mathrm{cr}}$ as expected.

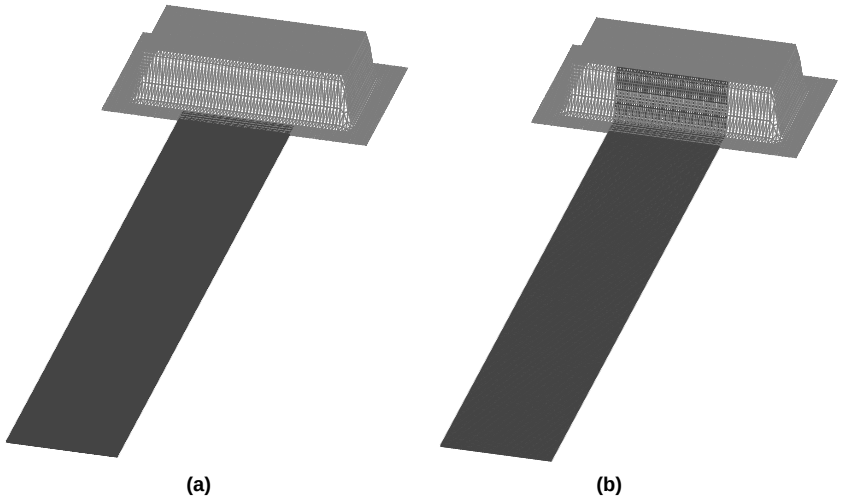

Fig. 10. The impact and contact of a deformable solid bar with a rigid target: (a) the determinant of the moment matrix in master domain before penetration; (b) the determinant of the moment matrix in master domain after penetration.

However, after the penetration occurs, one can observe from Fig. 10(b) that for the slave nodes that have penetrated into the master body, the determinant of the moment matrix of the master body is no longer 0, i.e., $\mathbf{x} \in \bar{\Omega}_s \cap \bar{\Omega}_m$, $\det\{\mathbf{M}_m(\mathbf{x}) \geqslant \epsilon_{cr}$, which is shown in Fig. 10(b) as the dark region moves up in z direction at the contact region. And this indicates the occurrence of penetration. The detailed computation results for the Taylor bar problem is presented in Section 6.

3. The Mathematical principle

In this section, the moment method is analyzed in details as we are trying to prove Proposition 2.1. To do so, we first define the continuous moment matrix

$$\mathbf{M}(\mathbf{x}) := \int_{\Omega} \mathbf{P}^{\mathrm{T}}\left(\frac{\mathbf{y}-\mathbf{x}}{\rho}\right)\phi_{\rho}(\mathbf{y}-\mathbf{x})\mathbf{P}\left(\frac{\mathbf{y}-\mathbf{x}}{\rho}\right)\mathrm{d}\Omega_y \tag{29}$$

and its discrete counterpart

$$\mathbf{M}^h(\mathbf{x}) = \sum_{\ell\in\Lambda} \mathbf{P}^{\mathrm{T}}\left(\frac{\mathbf{x}_\ell-\mathbf{x}}{\rho}\right)\phi_{\rho}(\mathbf{x}_\ell-\mathbf{x})\mathbf{P}\left(\frac{\mathbf{x}_\ell-\mathbf{x}}{\rho}\right)\Delta V_\ell. \tag{30}$$

Define

$$\langle f, g\rangle_y := \int_{\Omega} f(\mathbf{y}-\mathbf{x})g(\mathbf{y}-\mathbf{x})\phi_{\rho}(\mathbf{y}-\mathbf{x})\,\mathrm{d}\Omega_y. \tag{31}$$

It is almost trivial to show $\langle,\rangle$ is an inner product in $L^2(\Omega)$ $\forall \mathbf{x} \in \bar{\Omega}$. However, its discrete counterpart

$$\langle f, g\rangle^h := \sum_{I=1}^{\mathrm{NP}} f(\mathbf{x}_I-\mathbf{x})\phi_{\rho}(\mathbf{x}_I-\mathbf{x})g(\mathbf{x}_I-\mathbf{x})\Delta V_I \tag{32}$$

is not automatically an inner product, unless certain conditions on discretization are met. Eq. (29) can be rewritten as

$$\mathbf{M}(\mathbf{x}) := \begin{pmatrix} \langle P_1, P_1\rangle, & \langle P_1, P_2\rangle, & \dots & \langle P_1, P_m\rangle \\ \langle P_2, P_1\rangle, & \langle P_2, P_2\rangle, & \dots & \langle P_2, P_m\rangle \\ \vdots & & \ddots & \vdots \\ \langle P_m, P_1\rangle, & \langle P_m, P_2\rangle, & \dots & \langle P_m, P_m\rangle \end{pmatrix} \tag{33}$$

and the discrete version is

$$\mathbf{M}^h(\mathbf{x}) := \begin{pmatrix} \langle P_1, P_1\rangle^h, & \langle P_1, P_2\rangle^h, & \dots & \langle P_1, P_m\rangle^h \\ \langle P_2, P_1\rangle^h, & \langle P_2, P_2\rangle^h, & \dots & \langle P_2, P_m\rangle^h \\ \vdots & & \ddots & \vdots \\ \langle P_m, P_1\rangle^h, & \langle P_m, P_2\rangle^h, & \dots & \langle P_m, P_m\rangle^h \end{pmatrix}. \tag{34}$$

Since ϕ is positive and compact supported, for fixed $\mathbf{x}$, if $\text{meas}\{\text{supp}\{\phi_\rho(\mathbf{y}-\mathbf{x})\}\cap\Omega\} \neq 0$. the moment matrix should be positive definite, [2] i.e.,

$$\det\{\mathbf{M}(\mathbf{x})\} > 0. \tag{35}$$

Nevertheless, if $\text{meas}\{\text{supp}\{\phi_\rho(\mathbf{y}-\mathbf{x})\}\cap\Omega\} = 0$, then consequently

$$\int_\Omega P_I\left(\frac{\mathbf{y}-\mathbf{x}}{\rho}\right)\phi_\rho(\mathbf{y}-\mathbf{x})P_J\left(\frac{\mathbf{y}-\mathbf{x}}{\rho}\right)\mathrm{d}\Omega_y = 0 \tag{36}$$

the moment matrix will lose its positive definiteness. Mathematically speaking, the determinant of the moment matrix will become 0.

To quantify this notion, it can be stated as $\forall\mathbf{x} \notin \bar{\Omega}$

$$\text{meas}\{\text{supp}[\phi_\rho(\mathbf{y}-\mathbf{x})]\cap\Omega\} \to 0, \quad \rho \to 0 \tag{37}$$

$$\Rightarrow \det\{\mathbf{M}(\mathbf{x})\} \to 0, \tag{38}$$

On the other hand $\forall\mathbf{x} \in \bar{\Omega}$

$$\text{meas}\{\text{supp}[\phi_\rho(\mathbf{y}-\mathbf{x})]\cap\Omega\} > 0, \quad \text{if } \rho \neq 0, \tag{39}$$

$$\Rightarrow \det\{\mathbf{M}(\mathbf{x})\} > 0. \tag{40}$$

Therefore based on (38) and (40), one can identify spatial point by calculating the determinant of the moment matrix, to determine whether or not it belongs to $\bar{\Omega}$. However, in discrete cases, things have changed slightly, to recover the above property, we need the following notion of *admissible meshfree discretization*.

Definition 3.1 (*Admissible meshfree discretization* [27]). Given a positive window function, $\phi(x)$, and a set of independent functions, $\mathbf{P} = \{1, P_2, P_3, \dots, P_m\}$. An admissible meshfree discretization satisfies the following conditions:

1. Every particle of the distribution associates with a compact support

$$S_\ell := \{|\mathbf{x}-\mathbf{x}_\ell| \leqslant \rho_\ell\} \tag{41}$$

and the union of all the compact support, S_I, generates a covering for the domain $\bar{\Omega}$

$$\bar{\Omega} \subset S := \cup_{\ell\in\Lambda} S_\ell. \tag{42}$$

[2] A simple proof of this statement is given in Appendix A.

2. $\forall \mathbf{x} \in \bar{\Omega}$, $\exists k > 0$,

$$\mathbf{x} \in \cap_{\ell=1}^{k} \mathrm{supp}\{\phi(\mathbf{x}_\ell - \mathbf{x})\}, \tag{43}$$

where $N_{\min} \leqslant k \leqslant N_{\max}$ and $N_{\min}, N_{\max}$ are given.
3. The particle distribution should be non-degenerated.

We have the following theorem for the admissible particle distribution:

Theorem 3.1. *A necessary condition for an admissible, non-degenerated particle distribution is that* $\forall \mathbf{x} \in \bar{\Omega} \subset \mathbb{R}^n$,

$$\mathbf{x} \in \cap_{\ell=1}^{k} \mathrm{supp}\{\phi(\mathbf{x}_\ell - \mathbf{x})\}, \tag{44}$$

such that $\max\{m, n+1\} \leqslant N_{\min} \leqslant k$, *where m is the order of the polynomial basis, and n is the spatial dimension of the domain* Ω.

The following proof is partially due to [13].

Proof. Let us show the first part of statement, i.e., $m \leqslant N_{\min} \leqslant k$. The discrete moment matrix can be written as

$$\mathbf{M}^h(\mathbf{x}) = \begin{pmatrix} M^h_{11} & M^h_{12} & \cdots & M^h_{1m} \\ M^h_{21} & M^h_{22} & & M^h_{2m} \\ \vdots & & \ddots & \vdots \\ M^h_{m1} & M^h_{m2} & \cdots & M^h_{mm} \end{pmatrix}. \tag{45}$$

For fixed $x \in \Omega$, we assume that it is covered by only k compact supports of particles, numbering in the order $(\alpha_1, \alpha_2, \ldots, \alpha_k)$

$$M^h_{IJ}(\mathbf{x}) = \sum_{\ell=\alpha_1}^{\alpha_k} P_I\left(\frac{\mathbf{x}_\ell - \mathbf{x}}{\rho}\right) \phi_\rho(\mathbf{x}_\ell - \mathbf{x}) P_J\left(\frac{\mathbf{x}_\ell - \mathbf{x}}{\rho}\right) \Delta V_\ell. \tag{46}$$

Denote $P_I(\mathbf{x}_{\alpha_i}) := P_I\left(\frac{\mathbf{x}_{\alpha_i} - \mathbf{x}}{\rho}\right)$, $I = 1, 2, \ldots, m$. Then the moment matrix $\mathbf{M}^h(\mathbf{x})$ can be rewritten as

$$\mathbf{M}^h(\mathbf{x}) = \boldsymbol{\Pi}^h \cdot \boldsymbol{\Phi} \cdot \boldsymbol{\Pi}^{h^{\mathrm{T}}} = \begin{pmatrix} P_1(\mathbf{x}_{\alpha_1}) & P_1(\mathbf{x}_{\alpha_2}) & \cdots & P_1(\mathbf{x}_{\alpha_k}) \\ P_2(\mathbf{x}_{\alpha_1}) & P_2(\mathbf{x}_{\alpha_2}) & \cdots & P_2(\mathbf{x}_{\alpha_k}) \\ \vdots & \vdots & \ddots & \vdots \\ P_m(\mathbf{x}_{\alpha_1}) & P_m(\mathbf{x}_{\alpha_2}) & \cdots & P_m(\mathbf{x}_{\alpha_k}) \end{pmatrix}$$
$$\cdot \begin{pmatrix} \phi_\rho(\mathbf{x}_{\alpha_1} - \mathbf{x}) & 0 & \cdots & 0 \\ 0 & \phi_\rho(\mathbf{x}_{\alpha_2} - \mathbf{x}) & \cdots & 0 \\ \vdots & \vdots & \ddots & \vdots \\ 0 & 0 & \cdots & \phi_\rho(\mathbf{x}_{\alpha_k} - \mathbf{x}) \end{pmatrix} \cdot \begin{pmatrix} P_1(\mathbf{x}_{\alpha_1}) & P_2(\mathbf{x}_{\alpha_1}) & \cdots & P_m(\mathbf{x}_{\alpha_1}) \\ P_1(\mathbf{x}_{\alpha_2}) & P_2(\mathbf{x}_{\alpha_2}) & \cdots & P_m(\mathbf{x}_{\alpha_2}) \\ \vdots & \vdots & \ddots & \vdots \\ P_1(\mathbf{x}_{\alpha_k}) & P_2(\mathbf{x}_{\alpha_k}) & \cdots & P_m(\mathbf{x}_{\alpha_k}) \end{pmatrix}. \tag{47}$$

From Eq. (47), one can find that the rank of $\boldsymbol{\Pi}^h$ is at most k, and hence the rank of the moment matrix is at most k as well. Then the positive definiteness of the moment matrix, $\mathbf{M}^h(\mathbf{x}) > 0$, requires $k \geqslant m$.

In the second part of the proof, we show that $k \geqslant n+1$ is a necessary condition through an example. Let $\bar{\Omega} \subset \mathbb{R}^2$ and $\mathbf{P}(\mathbf{x}) = \{1, xy\}$, and assume that some points, $(x, y) \in \Omega$, are covered by compact supports of only two particles, i.e., $k = 2$. It is obvious that $k \geqslant m$ but $k < n+1$. Here $\boldsymbol{\Pi}$ matrix reads as

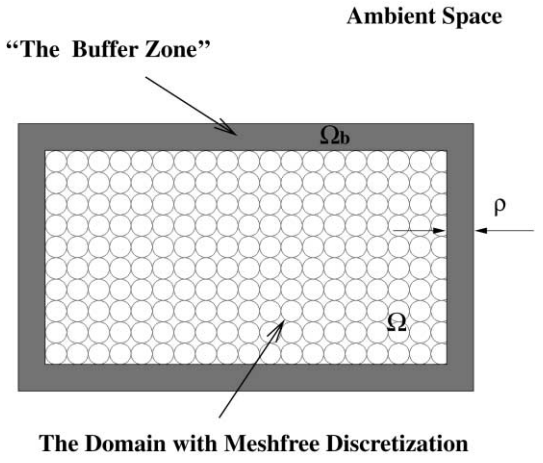

Fig. 11. An illustration of the "buffer zone".

$$\boldsymbol{\Pi}(\mathbf{x}) = \begin{pmatrix} 1 & 1 \\ (x_1 - x)(y_1 - y) & (x_2 - x)(y_2 - y) \end{pmatrix}. \tag{48}$$

Choose $x = \frac{1}{2}(x_1 + x_2)$ and $y = \frac{1}{2}(y_1 + y_2)$. Then

$$\boldsymbol{\Pi}(\mathbf{x}) = \begin{pmatrix} 1 & 1 \\ \frac{1}{4}(x_1 - x_2)(y_1 - y_2) & \frac{1}{4}(x_1 - x_2)(y_1 - y_2) \end{pmatrix} \tag{49}$$

and the rank of **P** reduces to 1. Consequently, the resulting moment matrix will be singular. In fact, in two-dimensional case, each point in the domain must be covered by compact supports of, at least, three particles, which should form a non-degenerated triangle (i.e., the triangle must have non-zero value of the area). Likewise, in 3D case, each point in the domain should be in the domain of influence of, at least, four distinct particles, which form a non-degenerate tetrahedral volume. □

The above theorem implies a fact that any spatial point that is in, or close to (in the buffer zone) the domain that has an admissible meshfree discretization, the determinant of the moment matrix at that point will have a positive value, because the necessary condition can be satisfied. Otherwise the moment matrix will not be positive definite, because for the spatial point that is away from the domain, there will not be sufficient particles (or simply no particles at all) to be able to cover such outside point, and consequently the above necessary condition will fail, and the determinant of the moment matrix will cease to be a finite positive number. This is precisely the claim stated in Proposition 2.1. It is this fact that provides a natural criterion to distinguish interior points and exterior points of any domain that has an admissible meshfree discretization.

We would like to make a few comments on the role of the buffer zone. First, the buffer zone is a regularization mechanism, which provide a useful agent in numerical computation to avoid ill conditioning in contact simulations. Second, when we refine the particle distribution, or in other words, decreasing the support size of the window function, the buffer zone will diminish quickly. [3] As a matter of fact, if one chooses $\delta = \rho$, and the average radius of the compact support as $\rho = \sqrt{\rho_x^2 + \rho_y^2 + \rho_z^2}$, then $\text{dist}\{\{\bar{\Omega}\}, \mathbf{x}\} > \delta$ leads to $\det\{\mathbf{M}(\mathbf{x})\} \to 0$ immediately. One can immediately identify the buffer zone as the region that

$$\{\mathbf{x} \,|\, 0 < \text{dist}\{\bar{\Omega}, \mathbf{x}\} < \rho\}. \tag{50}$$

Fig. 11 is a schematic illustration of the buffer zone of Example 2.2 in Section 2.

[3] When the density of a particle distribution increases, it is always assumed that at the same time the support size of the window function decreases, such that the number of the particles inside a compact support, or inside the domain of influence remain approximately the same as before.

4. Weak form, discretization, and constitutive model

A total Lagrangian formulation is adopted in the numerical computation. Followed the standard convention that $\mathbf{x}$ denotes the spatial coordinate of a material point and $\mathbf{X}$ denotes the referential coordinate of the same material point, the displacement of the material point is defined as

$$\mathbf{u} := \mathbf{x} - \mathbf{X}, \tag{51}$$

and the deformation gradient is given by,

$$\mathbf{F} := \frac{\partial \mathbf{x}}{\partial \mathbf{X}}. \tag{52}$$

In large inelastic deformation, the deformation gradient, $\mathbf{F}$, can be decomposed as

$$\mathbf{F} = \mathbf{F}^e \cdot \mathbf{F}^p, \tag{53}$$

where $\mathbf{F}^e$ describes the elastic deformation and rigid body rotation and $\mathbf{F}^p$ describes the inelastic deformation, The rate of deformation tensor, $\mathbf{D}$, and the spin tensor, $\mathbf{W}$, are the symmetry part and anti-symmetry part of the spatial velocity gradient $\mathbf{L} = \dot{\mathbf{F}} \cdot \mathbf{F}^{-1}$, i.e.,

$$\mathbf{D} + \mathbf{W} = \dot{\mathbf{F}} \cdot \mathbf{F}^{-1} = \dot{\mathbf{F}}^e \cdot \mathbf{F}^{e^{-1}} + \mathbf{F}^e \cdot \dot{\mathbf{F}}^p \cdot \mathbf{F}^{p^{-1}} \cdot \mathbf{F}^{e^{-1}} \tag{54}$$

by using the fact that $\dot{\mathbf{F}} = \dot{\mathbf{F}}^e \mathbf{F}^p + \mathbf{F}^e \dot{\mathbf{F}}^p$ and $\mathbf{F}^{-1} = \mathbf{F}^{p^{-1}} \mathbf{F}^{e^{-1}}$. Consequently, the following decomposition holds:

$$\mathbf{D}^e + \mathbf{W}^e = \dot{\mathbf{F}}^e \cdot \mathbf{F}^{e^{-1}}, \tag{55}$$

$$\mathbf{D}^p + \mathbf{W}^p = \mathbf{F}^e \cdot \dot{\mathbf{F}}^p \cdot \mathbf{F}^{p^{-1}} \cdot \mathbf{F}^{e^{-1}}. \tag{56}$$

A weak form of the balance of linear momentum at finite strain can be written as

$$\boxed{\int_{\Omega_0} \mathbf{P} : \delta \mathbf{F}^{\mathrm{T}} \, \mathrm{d}\Omega = \int_{\Omega_0} \rho_0 \mathbf{B} \cdot \delta \mathbf{u} \, \mathrm{d}\Omega + \int_{\Gamma^{\mathrm{trac}}} \mathbf{T} \cdot \delta \mathbf{u} \, \mathrm{d}S - \int_{\Omega_0} \rho_0 \frac{\partial^2 \mathbf{u}}{\partial t^2} \delta \mathbf{u} \, \mathrm{d}\Omega,} \tag{57}$$

where $\mathbf{B}$ is the body force, and $\mathbf{T}$ is the prescribed traction on the traction boundary, Γ^{trac}, and $\mathbf{P}$ denotes the first Piola–Kirchhoff stress tensor, which can be related to the Kirchhoff stress tensor as $\boldsymbol{\tau} = \mathbf{F} \cdot \mathbf{P}$. And

$$\overset{\triangledown}{\boldsymbol{\tau}} = \mathbf{C} : [\mathbf{D} - \mathbf{D}^p], \tag{58}$$

where $\mathbf{C}$ is the elastic stiffness tensor, and $\overset{\triangledown}{\boldsymbol{\tau}}$ is the Jaumann rate of the Kirchhoff stress, which is defined as

$$\overset{\triangledown}{\boldsymbol{\tau}} := \dot{\boldsymbol{\tau}} - \mathbf{W} \cdot \boldsymbol{\tau} + \boldsymbol{\tau} \cdot \mathbf{W}. \tag{59}$$

Let

$$\mathbf{u}^h(X, t) = \sum_{I \in \mathcal{A}} N_I(X) \mathbf{d}_I(t). \tag{60}$$

Then discrete weak formulations

$$\boxed{\int_{\Omega_0} \mathbf{P}_{n+1} : \delta \mathbf{F}^{\mathrm{T}} \, \mathrm{d}\Omega = \int_{\Omega_0} \rho_0 (\mathbf{B}_{n+1} - \mathbf{a}_{n+1}) \cdot \delta \mathbf{u} \, \mathrm{d}\Omega + \int_{\Gamma^{\mathrm{trac}}} \mathbf{T}_{n+1} \cdot \delta \mathbf{u} \, \mathrm{d}S} \tag{61}$$

and central difference scheme lead to the following discrete equations of motion:

$$\mathbf{a}_{n+1} = \mathscr{M}^{-1} \left(\mathbf{f}^{\mathrm{ext}}_{n+1} - \mathbf{f}^{\mathrm{int}}_{n+1} \right), \tag{62}$$

$$\mathbf{v}_{n+1} = \mathbf{v}_n + \tfrac{1}{2} \Delta t (\mathbf{a}_n + \mathbf{a}_{n+1}), \tag{63}$$

$$\mathbf{u}_{n+1} = \mathbf{u}_n + \Delta t \mathbf{v}_n + \tfrac{1}{2}\Delta t^2 \mathbf{a}_n, \tag{64}$$

where $\mathbf{a}_n$ is accelaration, $\mathbf{v}_n$ the velocity and $\mathbf{u}_n$ is displacement:

$$\mathbf{u}_n^h = \{\mathbf{d}_1, \mathbf{d}_2, \ldots, \mathbf{d}_{\mathrm{NP}}\}_n^{\mathrm{T}}, \tag{65}$$

$$\mathbf{v}_n^h = \{\dot{\mathbf{d}}_1, \dot{\mathbf{d}}_2, \ldots, \dot{\mathbf{d}}_{\mathrm{NP}}\}_n^{\mathrm{T}}, \tag{66}$$

$$\mathbf{a}_n^h = \{\ddot{\mathbf{d}}_1, \ddot{\mathbf{d}}_2, \ldots, \ddot{\mathbf{d}}_{\mathrm{NP}}\}_n^{\mathrm{T}}, \tag{67}$$

$$\mathbf{f}_n^{\mathrm{ext}} = \{\mathbf{f}_1^{\mathrm{ext}}, \mathbf{f}_2^{\mathrm{ext}}, \ldots, \mathbf{f}_{\mathrm{NP}}^{\mathrm{ext}}\}_n^{\mathrm{T}}, \tag{68}$$

$$\mathbf{f}_n^{\mathrm{int}} = \{\mathbf{f}_1^{\mathrm{int}}, \mathbf{f}_2^{\mathrm{int}}, \ldots, \mathbf{f}_{\mathrm{NP}}^{\mathrm{int}}\}_n^{\mathrm{T}}. \tag{69}$$

In (62), $\mathscr{M}$ is the mass matrix. The lumped mass matrix is used in computations, i.e.,

$$\mathscr{M}_{IJ} = \int_{\Omega_0} \rho_0 N_I N_J \,\mathrm{d}\Omega \approx \begin{cases} \int_{\Omega_0} \rho_0 N_I \,\mathrm{d}\Omega & I = J, \\ 0 & I \neq J. \end{cases} \tag{70}$$

The components of mechanical force are given as follows

$$\mathbf{f}_I^{\mathrm{ext}} = \int_{\Gamma^{\mathrm{trac}}} T_i(X,t) N_I \mathbf{e}_i \,\mathrm{d}S + \int_{\Omega_0} \rho_0 B_i(X,t) N_I(X) \mathbf{e}_i \,\mathrm{d}\Omega, \tag{71}$$

$$\mathbf{f}_I^{\mathrm{int}} = \int_{\Omega_0} P_{Ji}^h \frac{\partial N_I}{\partial X_J} \mathbf{e}_i \,\mathrm{d}\Omega. \tag{72}$$

A von Mises type (J_2) overstress viscoplastic model is considered, i.e.

$$\mathbf{D}^p = \left(\frac{3\dot{\bar{\epsilon}}}{2\bar{\sigma}}\right)\mathbf{s}', \tag{73}$$

where

$$\mathbf{s} = \boldsymbol{\tau} - \tfrac{1}{3}\mathrm{tr}(\boldsymbol{\tau})\mathbf{1} \tag{74}$$

$$\mathbf{s}' = \mathbf{s} - \boldsymbol{\alpha}, \tag{75}$$

$$\bar{\sigma}^2 = \frac{3}{2}\mathbf{s}' : \mathbf{s}', \tag{76}$$

and

$$\bar{\epsilon} = \int_0^t \left[\frac{\mathbf{D}^p : \mathbf{D}^p}{\mathbf{p} : \mathbf{p}}\right]^{1/2} \mathrm{d}t, \tag{77}$$

$$\mathbf{p} := \frac{3}{2}\frac{\mathbf{s}'}{\bar{\sigma}}. \tag{78}$$

A power law governed viscoplastic constitutive law is adopted to model the deformed solid (see [31,32]).

$$\dot{\bar{\epsilon}} = \dot{\epsilon}_0 \left[\frac{\bar{\sigma}}{g(\bar{\epsilon})} \right]^{1/m}, \tag{79}$$

$$g(\bar{\epsilon}) = \sigma_0 \frac{(1 + \bar{\epsilon}/\epsilon_0)^N}{1 + (\bar{\epsilon}/\epsilon_1)^2}, \tag{80}$$

where m and N are the power indices. The evolution of the back stress at finite strain has a form of the Prager–Ziegler relation,

$$\overset{\triangledown}{\boldsymbol{\alpha}} = b\mathbf{D}^p. \tag{81}$$

Peirce et al.'s [33] rate tangent modulus method is used to update state variables,

$$\dot{\bar{\epsilon}}_{n+1} = \dot{\bar{\epsilon}}_n + \Delta t_n \left[\left. \frac{\partial \dot{\bar{\epsilon}}}{\partial \bar{\sigma}} \right|_n \dot{\bar{\sigma}}_\theta + \left. \frac{\partial \dot{\bar{\epsilon}}}{\partial \bar{\epsilon}} \right|_n \dot{\bar{\epsilon}}_\theta \right] \tag{82}$$

and

$$\dot{\bar{\epsilon}}_\theta \approx \frac{\dot{\bar{\epsilon}}_n}{1 + \xi_\theta} + \frac{1}{H_\theta} \frac{\xi_\theta}{1 + \xi_\theta} \mathbf{P}_\theta : \mathbf{D}_\theta, \tag{83}$$

where

$$H_\theta \approx \frac{3E}{2(1+\nu)} + b\mathbf{p} : \mathbf{p} - \left. \frac{\partial \dot{\bar{\epsilon}}/\partial \bar{\epsilon}}{\partial \dot{\bar{\epsilon}}/\partial \bar{\sigma}} \right|_n, \tag{84}$$

$$\mathbf{P} := \mathbf{C} : \mathbf{p}, \tag{85}$$

$$\xi_\theta \approx \theta \Delta t \left(\frac{\partial \dot{\bar{\epsilon}}}{\partial \bar{\sigma}} \right)_n H_\theta. \tag{86}$$

The Jaumann rate of the Kirchhoff stress is updated as

$$\overset{\triangledown}{\boldsymbol{\tau}}_\theta = \mathbf{C}_\theta^{\tan} : \mathbf{D}_\theta - \frac{\dot{\bar{\epsilon}}_n}{1 + \xi_n} \mathbf{P}_\theta, \tag{87}$$

$$\mathbf{C}_\theta^{\tan} = \mathbf{C} - \frac{\xi_n}{1 + \xi_n} \frac{1}{H_\theta} \mathbf{P}_\theta \otimes \mathbf{P}_\theta. \tag{88}$$

For the detailed meshfree implementation, readers are referred to the papers by Li et al. [18,19].

5. Implementation of friction/impenetrability conditions

Contact problem are characterized by the so-called impenetrability condition that needs to be enforced during the computation. In other words, no inter-penetration is allowed between two contacting objects. There are two types of approaches to enforce the impenetrability condition: one is the Lagrangian multiplier method and penalty method (e.g., [14,17]); the other is the exact enforcement of the penetration condition in a single time step (e.g., [11,16]). The first approach is more suitable for stationary contact

problems, whereas the second approach is suitable for impact-contact problems. In this paper, the second approach is adopted because we are only interested in impact-contact problem here.

For illustration purpose, we consider the case that the master body is stationary. The contact algorithm begins with the prediction of the position of the slave body at time step n, i.e., finding $\bar{\Omega}_s(t_n)$. The contact-detection algorithm is then used to search all the inter-penetration particles as described in Section 2. After all the penetrated particles have been detected, an auxiliary list is generated for those particles. The next step is to calculate the normal gap and tangential velocity between the intrusion slave particle and the closest master surface. In 2D case, the following formulas are used (see Fig. 12),

$$g_j = (\mathbf{x}_{s(j)} - \mathbf{x}_{m(i)}) \cdot \mathbf{n}_i, \tag{89}$$

$$\mathbf{v}_{t(j)} = (\mathbf{v}_{s(j)} \cdot \mathbf{n}_i)\mathbf{t}_i, \tag{90}$$

where

$$\mathbf{t}_i = \frac{(\mathbf{x}_{m(i+1)} - \mathbf{x}_{m(i)})}{\|\mathbf{x}_{m(i+1)} - \mathbf{x}_{m(i)}\|}, \tag{91}$$

$$\mathbf{n}_i = \mathbf{e}_3 \times \mathbf{t}_i, \tag{92}$$

and $\mathbf{e}_3$ is the unit vector pointing outward from the plane. We would like to comment that in contrast with the conventional contact algorithm, there is no need for global vector operation search to match a slave penetration particle and a master surface segment in the meshfree contact algorithm. Since usually the master surface segment should be within the support of the particular slave particle, a comparison with scalar criterion is sufficient. In actual computation, there are at most three master surface segments may intersect a specified slave particle.

We then can calculate the contact forces that are required to prevent inter-penetration. For central difference scheme, we have

$$\mathbf{f}_{n(j)} = \frac{2M_{s(j)}g_j}{\Delta t^2}\mathbf{n}_i = f_{n(j)}\mathbf{n}_i, \tag{93}$$

where $\mathbf{n}_i$ is the out normal vector of ith master segment that is in match with the jth penetrated slave particle.

On the tangential direction of the contact surface, the classical Coulomb friction model is adopted in modeling friction between slave body and master body. To enforce the stick condition, we have

$$\mathbf{f}^{\text{stick}}_{t(j)} = -\frac{M_{s(j)}}{\Delta t}\mathbf{v}_{t(j)}. \tag{94}$$

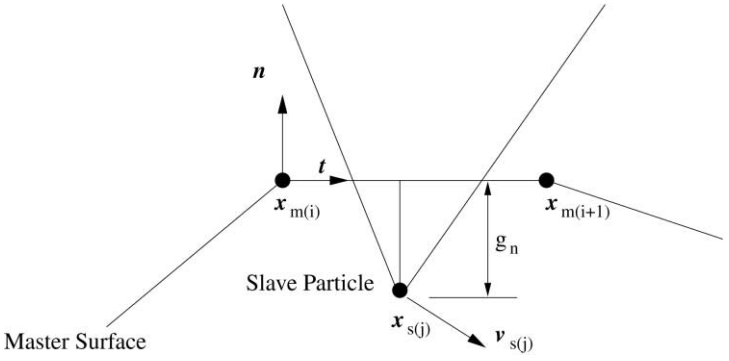

Fig. 12. A match pair of a master segment and a slave particle.

The tangential force exerted by master surface to a slave particle can not exceed the tangent force limit the interface can hold. After reaching the tangential force limit, a slip condition, or kinetic friction force should be applied,

$$\mathbf{f}_{t(j)}^{\text{slip}} = -|\mu_k f_{n(j)}| \frac{\mathbf{v}_{t(j)}}{\|\mathbf{v}_{t(j)}\|}. \tag{95}$$

In general

$$\mathbf{f}_{t(j)} = -\min\left(\mu_k f_{n(j)}, \|\mathbf{f}_{t(j)}^{\text{stick}}\|\right) \frac{\mathbf{v}_{t(j)}}{\|\mathbf{v}_{t(j)}\|}. \tag{96}$$

The force vectors calculated above are the exact nodal force vector for each penetrating particle to satisfy the impenetrability condition and friction condition at interface. If one uses meshfree interpolants in the numerical computation, one has to re-distribute such nodal-exact force to a non-local "fictitious force". The rational and the procedure is derived from the virtual work principle at the interface

$$\begin{aligned}\delta W^{\text{contact}} &= \int_{\Gamma^{\text{contact}}} \mathbf{f} \cdot \delta\mathbf{u}\, \mathrm{d}S = \int_{\Gamma^{\text{contact}}} \sum_{J\in\Lambda} \mathbf{f}_J \hat{\delta}(\mathbf{x}-\mathbf{x}_J) \cdot \delta\mathbf{u}\, \mathrm{d}S = \sum_{J\in\Lambda} \mathbf{f}_J \sum_{I\in\Lambda} N_I(\mathbf{x}_J)\delta\mathbf{d}_I \\ &= \sum_{I\in\Lambda} \left(\sum_{J\in\Lambda} N_I(\mathbf{x}_J)\mathbf{f}_J \right) \delta\mathbf{d}_I = \sum_{I\in\Lambda} \bar{\mathbf{f}}_I \cdot \delta\mathbf{d}_I,\end{aligned} \tag{97}$$

where $\hat{\delta}(\mathbf{x})$ is the standard Kronecker Delta function; $\mathbf{d}_I$, $I \in \Lambda$ is the fictitious nodal displacement vector. Hence, the fictitious force vector at the particle, I, is

$$\bar{\mathbf{f}}_I = \sum_{J\in\Lambda} \mathbf{f}_J N_I(\mathbf{x}_J). \tag{98}$$

In finite element interpolation, $N_I(\mathbf{x}_J) = \hat{\delta}_{IJ}$, we recover the exact nodal force vector from (98),

$$\bar{\mathbf{f}}_I = \sum_{J\in\Lambda} \mathbf{f}_J N_I(\mathbf{x}_J) = \sum_{J\in\Lambda} \mathbf{f}_J \hat{\delta}_{IJ} = \mathbf{f}_I. \tag{99}$$

6. Numerical examples

To validate the contact-detection algorithm, numerical computations have been carried out testing its viability in computation. We consider the impact problem of the Taylor bar described in Section 2, and the exact problem statement is described in Fig. 13. The projectile is a cylindrical rod with radius, $R_s = 5$ mm, and height, $L = 60$ mm and the rigid block has radius $R_m = 12$ and 10 mm in height. The material's constitutive model is chosen as the viscoplastic solid described in Section 4. The following material constants are listed in Table 1. Since the problem is axi-symmetric, only half of the cylinder is modelled in actual computation. Two sets of computations have been carried out: one via meshfree method and the other via finite element method (FEM). In meshfree computation, a total of 11,191 particles are used in discretization of the Taylor bar, and 1661 particles are used to form the meshfree discretization of the rigid target. In time integration, the time step size is chosen as $\Delta t = 2.5 \times 10^{-9}$ s. The dilation parameters in slave body are selected as $\rho_x = 2.24\Delta x, \rho_y = 2.24\Delta y$ and $\Delta x = \Delta y = 0.166667$ mm; accordingly in master body, they are $\rho_x = 2.24\Delta x, \rho_y = 2.24\Delta y, \Delta x = 0.08$ mm $\Delta y = 1.0$ mm. Coulomb friction coefficient is chosen as $\mu = 0.1$, and the threshold value for contact-detection is set at $\epsilon_{\text{cr}} = 5 \times 10^{-10}$. A sequence of snap shots are taken from the numerical results at different time instance, and shown in Fig. 14(a)–(d).

The same meshfree contact-detection algorithm can also be used in finite element computation as well by assuming the existing finite element grid is a valid particle distribution. In this particular example, we only need to check the intrusion of projectile into the rigid target; therefore, the projectile, i.e., the Taylor bar is discretized via finite element mesh, and there is a meshfree particle distribution on rigid target. In general,

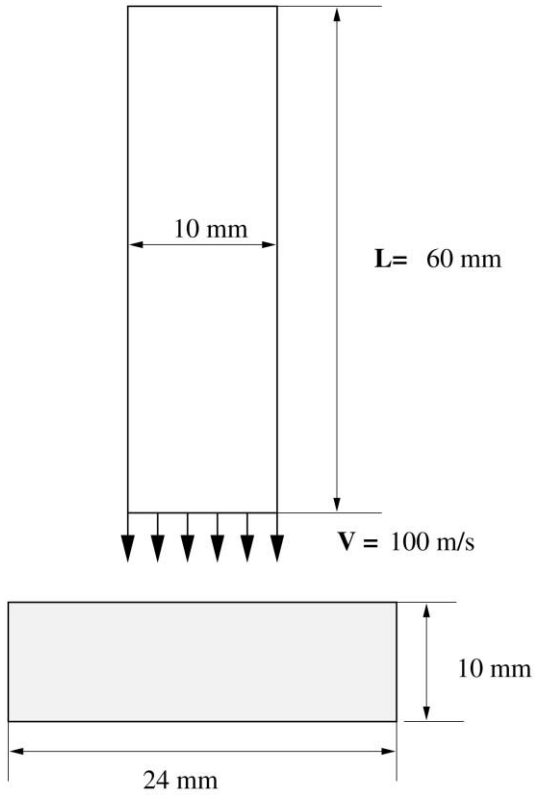

Fig. 13. The statement of the Taylor bar problem.

Table 1
The list of material constants

Mass density	$\rho = 7800$ Kg/m^3
Young's modulus	$E = 2110$ MPa
Poisson's ratio	$\mu = 0.3$
Yield stress	$\sigma_0 = 460$ MPa
Hardening index	$N = 0.1$
Hardening index	$m = 0.01$
Material constant	$\epsilon_0 = 2.18 \times 10^{-3}$
Material constant	$\epsilon_1 = 100\epsilon_0$
Material constant	$\dot{\epsilon}_0 = 0.0021/\text{s}$

one can construct moment matrix upon the finite element mesh by assign appropriate dilation parameter for the nodal distribution.

In finite element computation, the classical CST4 element are used in simulation, i.e., a quadrilateral box consisting of four diagonally crossed triangle elements. A total of 21,991 nodes and 43,200 elements are used in computation (there are 10,800 quadrilateral boxes). The time step increment is chosen to be $\Delta t = 6.25 \times 10^{-10}$ s due to the small size of the element. Similar deformation patterns to that of meshfree computation (Fig. 14) are observed (see Fig. 15). One may observe from both Figs. 14 and 15 that there is a mushroom region at the bottom of the Taylor bar, and there is a visible, cup shape shear band formation across the radius direction of the Taylor bar, which is due to plastic deformation during the high speed impact. Furthermore, numerical simulations in both meshfree and finite element computations predict the separation of the projectile and the rigid target at the edge of the Taylor bar in the contact region, which is an indication of excellent performance of the contact-detection algorithm. The results reported here are

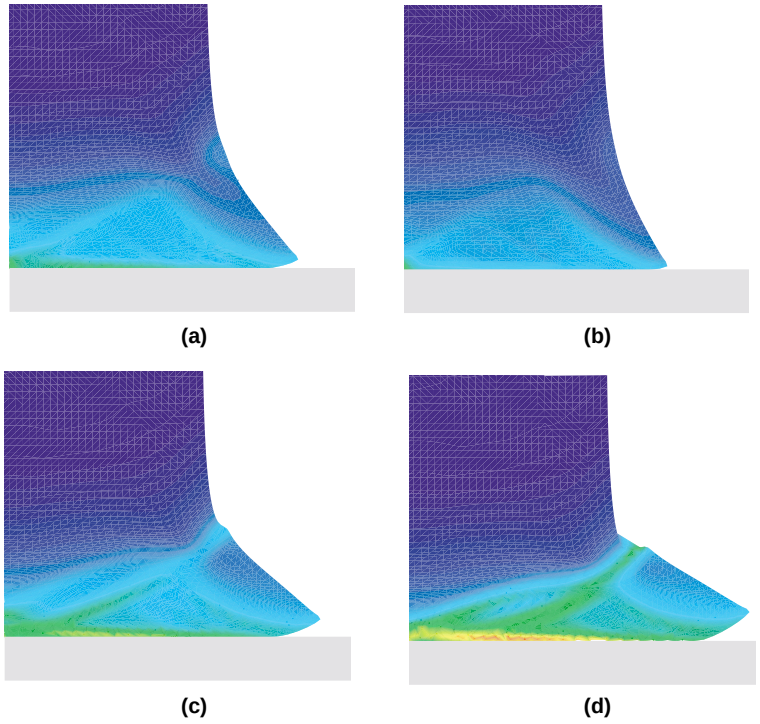

Fig. 14. The impact sequence of the Taylor bar via RKPM: (a) $t = 12.0$ μs; (b) $t = 16.0$ μs; (c) $t = 20.0$ μs; (d) $t = 24.0$ μs.

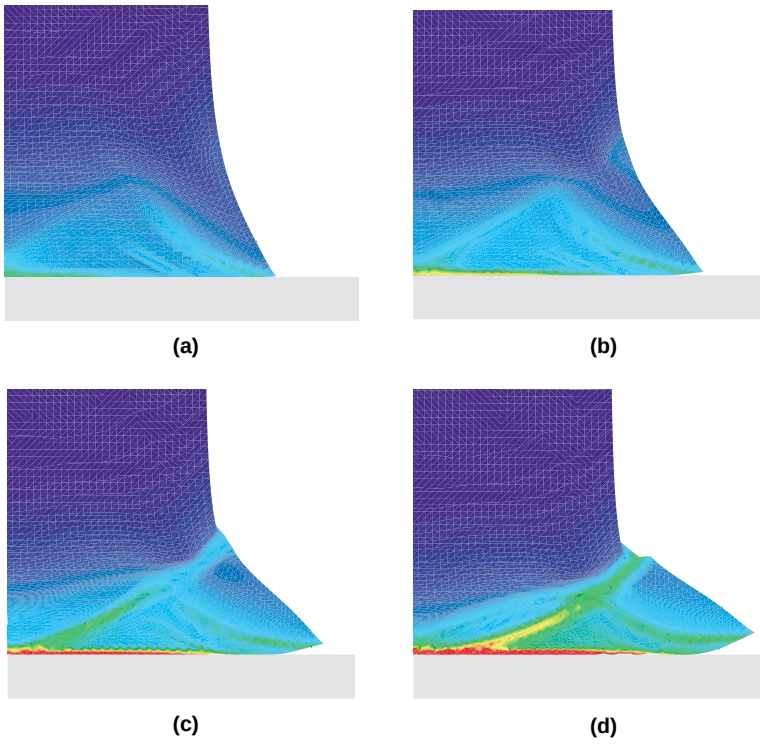

Fig. 15. The impact sequence of the Taylor bar via FEM: (a) $t = 12.0$ μs; (b) $t = 16.0$ μs; (c) $t = 20.0$ μs; (d) $t = 24.0$ μs.

consistent with the numerical results reported early by Batra and Stevens [4], or by Benson [9]) in finite element computations, in which the conventional contact-detection algorithm, such as Benson–Hallquist algorithm is used.

7. Concluding remarks

In this paper, a new contact-detection algorithm has been proposed based on the moment method in meshfree discretization. In fact, this moment method is essential to meshfree surface fitting, and meshfree volume representation. The mathematical principle of such contact-detection algorithm is that the determinant of the moment matrix can automatically determine Lagrangian movement of the continuum, and can be used to detect a spatial point on whether or not it belongs to the object of interest. The unique advantage of such contact-detection algorithm is that it is a simple, scalar criterion, which provides an effective solution to develop scalable contact searching algorithm in parallel computations. In addition, meshfree contact-detection algorithm is a Lagrangian approach in nature, which can automatically track the movement of a deformed continuum, thus, one can accurately detect the contact/penetration without solving any equations; this is in sharp contrast to the current FEM contact-detection algorithms that have to solve some complicated geometric equations to determine the intersection between a moving surface and a point.

The proposed contact-detection algorithm is implemented to simulate a Taylor bar impact problem. Good numerical solutions are obtained, which validate the proposed contact-detection algorithm. Moreover, such contact-detection algorithm can be extensively used in other contact scenarios as well, such as stationary contact detection, or self-contact detection. As a matter of fact, these are the issues that are in our current agenda.

Acknowledgements

This work is supported by grants from the the Army Research Office, and National Science Foundations. It is also sponsored in part by the Army High Performance Computing Research Center under the auspices of the Department of the Army, Army Research Laboratory cooperative agreement number DAAH04-95-2-003/contract number DAAH04-95-C-0008, the content of which does not necessarily reflect the position or the policy of the government, and no official endorsement should be inferred.

Appendix A. The positive definiteness of the moment matrix

In what follows, we show that the RKPM moment matrix,

$$\mathbf{M}(\mathbf{x}) := \begin{pmatrix} \langle P_1, P_1\rangle, & \langle P_1, P_2\rangle, & \dots & \langle P_1, P_m\rangle \\ \langle P_2, P_1\rangle, & \langle P_2, P_2\rangle, & \dots & \langle P_2, P_m\rangle \\ \vdots & & \ddots & \vdots \\ \langle P_m, P_1\rangle, & \langle P_m, P_2\rangle, & \dots & \langle P_m, P_m\rangle \end{pmatrix}, \tag{A.1}$$

is positive definite, if $x \in \Omega$. The standard procedure is followed here, nevertheless, we refer readers to Mitrinović [30] for a general treatment.

Since the window function is defined as

$$\phi_\rho(\mathbf{y}-\mathbf{x}) = \begin{cases} > 0, & \mathbf{y} \in \operatorname{supp}\{\phi_\rho(\mathbf{y}-\mathbf{x})\}, \\ = 0, & \mathbf{y} \notin \operatorname{supp}\{\phi_\rho(\mathbf{y}-\mathbf{x})\}, \end{cases} \tag{A.2}$$

the operation

$$\langle f, g\rangle_y = \int_\Omega f(\mathbf{y}-\mathbf{x})\phi_\rho(\mathbf{y}-\mathbf{x})g(\mathbf{y}-\mathbf{x})\,\mathrm{d}\Omega \tag{A.3}$$

defines an inner product in $L^2(\Omega)$, provided that $x \in \Omega$. [4] We first show $\det\{\mathbf{M}\} \neq 0$. Assume $\det\{\mathbf{M}\} = 0$. Then one can find a set of nontrivial constants, $z_1, z_2, \ldots, z_m$, such that

$$\begin{aligned}
&\langle P_1, P_1\rangle z_1 + \langle P_1, P_2\rangle z_2 + \cdots + \langle P_1, P_m\rangle z_m = 0,\\
&\langle P_2, P_1\rangle z_1 + \langle P_2, P_2\rangle z_2 + \cdots + \langle P_2, P_m\rangle z_m = 0, \qquad (A.4)\\
&\qquad\qquad \cdots \qquad (A.5)\\
&\langle P_m, P_1\rangle z_1 + \langle P_m, P_2\rangle z_2 + \cdots + \langle P_m, P_m\rangle z_m = 0.
\end{aligned}$$

Eq. (A.4) can also be expressed as

$$\begin{aligned}
&\langle P_1, P_1 z_1, + P_2 z_2 + \cdots + P_m z_m\rangle = 0,\\
&\langle P_2, P_1 z_1, + P_2 z_2 + \cdots + P_m z_m\rangle = 0,\\
&\qquad\qquad \cdots\\
&\langle P_m, P_1 z_1, + P_2 z_2 + \cdots + P_m z_m\rangle = 0.
\end{aligned} \qquad (A.6)$$

Multiplying the ith equation in (A.6) with z_i and summing them together yields

$$\langle P_1 z_1 + P_2 z_2 + \cdots + P_m z_m, P_1 z_1 + P_2 z_2 + \cdots + P_m z_m\rangle = 0, \qquad (A.7)$$

which leads to

$$P_1 z_1 + P_2 z_2 + \cdots + P_m z_m = 0. \qquad (A.8)$$

Since the polynomial basis $(P_1, P_2, \ldots, P_m)$ is linear independent by definition, (A.8) leads to contradiction. Thus

$$\det\{\mathbf{M}\} \neq 0. \qquad (A.9)$$

Now we show $\det\{\mathbf{M}\} > 0$. Since $(z_1, z_2, \ldots, z_m)$ is nontrivial (not every of them equals to zero) and $(P_1, P_2, \ldots, P_m)$ are independent. We must have

$$\langle P_1 z_1 + P_2 z_2 + \cdots + P_m z_m, P_1 z_1 + P_2 z_2 + \cdots + P_m z_m\rangle > 0. \qquad (A.10)$$

In other words

$$\sum_{i,j}^{m} \langle P_i, P_j\rangle z_i z_j = \sum_{i,j}^{m} M_{ij} z_i z_j > 0. \qquad (A.11)$$

Since $M_{ij} = M_{ji}$ and M_{ij} are real, one can conclude immediately that

$$\det\{\mathbf{M}(\mathbf{x})\} > 0 \quad \forall \mathbf{x} \in \bar{\Omega}. \qquad (A.12)$$

References

[1] S.N. Atluri, T. Zhu, A new meshfree local Petrov–Galerkin (mlpg) approach in computational mechanics, Comput. Mech. 22 (1998) 117–127.

[2] S.N. Atluri, T. Zhu, A meshless local Petrov–Galerkin (mlpg) approach for solving problems in elasto-statics, Comput. Mech. 25 (2) (2000) 169–179.

[3] S.W. Attaway, B.A. Hendrickson, S.J. Plimpton, D.R. Gardner, C.T. Vaughan, K.H. Brown, M.W. Heinstein, A parallel contact detection algorithm for transient solid dynamics simulations using pronto3d, Comput. Mech. 22 (1998) 143–159.

[4] R.C. Batra, J.B. Stevens, Adiabatic shear bands in axisymmetric impact and penetration problems, Comput. Methods Appl. Mech. Engrg. 151 (1998) 325–342.

[5] T. Belytschko, Y. Krongauz, D. Organ, M. Fleming, P. Krysl, Meshless methods: an overview and recent developments, Comput. Methods Appl. Mech. Engrg. 139 (1996) 3–48.

[4] Such that $\text{supp}\{\phi_\rho(\mathbf{y} - \mathbf{x}) \cap \Omega \neq \emptyset$, and $\int_\Omega \phi_\rho(\mathbf{y} - \mathbf{x})\, d\Omega > 0$.

[6] T. Belytschko, Y.Y. Lu, L. Gu, Element free galerkin methods, Int. J. Numer. Methods Engrg. 37 (1994) 229–256.
[7] T. Belytschko, M.O. Neal, Contact-impact by the pinball algorithm with penalty projection and lagrangian methods, Int. J. Numer. Methods Engrg. 31 (1991) 547–572.
[8] T. Belytschko, I.S. Yeh, The splitting pinball method for contact-impact problems, Comput. Methods Appl. Mech. Engrg. 105 (1993) 375–393.
[9] D.J. Benson, A mixture theory for contact in multi-material Eulerian formulations, Comput. Methods Appl. Mech. Engrg. 140 (1997) 59–86.
[10] D.J. Benson, J.O. Hallquist, A single surface contact algorithm for the post-buckling analysis of structures, Comput. Methods Appl. Mech. Engrg. 78 (1990) 141–163.
[11] G.T. Camacho, M. Ortiz, Adaptive lagrangian modelling of ballistic penetration of metallic targets, Comput. Methods Appl. Mech. Engrg. 142 (1997) 269–301.
[12] C.A. Duarte, J.T. Oden, An hp adaptive method using clouds, Comput. Methods Appl. Mech. Engrg. 139 (1996) 237–262.
[13] C.A. Duarte, J.T. Oden, Hp clouds – an hp meshless method, Numer. Methods Partial Diff. Eqs. 12 (1996) 673–705.
[14] J.O. Hallquist, G.L. Goudreau, D.J. Benson, Sliding interfaces with contact-impact in large-scale lagrangian computations, Comput. Methods Appl. Mech. Engrg. 5 (1985) 107–137.
[15] M.W. Heinstein, S.W. Attaway, F.J. Mello, J.W. Swegle, A general-purpose contact detection algorithm for nonlinear structural analysis codes, Technical Report, SAND92-2141, Sandia National Laboratories, Albuquerque NM, 1993.
[16] T.J.R. Hughes, R. Taylor, J. Sackman, A. Curnier, W. Kamoknukulchai, A finite element method for a class of contact-impact problem, Comput. Methods Appl. Mech. Engrg. 26 (1981) 331–362.
[17] N. Kikuchi, J.T. Oden, Contact Problems in Elasticity: A Study of Variational Inequalities and Finite Element Methods, SIAM, Philadelphia, 1988.
[18] S. Li, W. Hao, W.K. Liu, Numerical simulations of large deformation of thin shell structures using meshfree methods, Comput. Mech. 25 (2) (2000) 102–115.
[19] S. Li, W.K. Liu, Numerical simulations of strain localization in inelastic solids using meshfree methods, Int. J. Numer. Methods Engrg. 48 (9) (2000) 1285–1309.
[20] S. Li, W.K. Liu, Reproducing kernel hierarchical partition of unity part. I: Formulation and theory, Int. J. Numer. Methods Engrg. 45 (1999) 251–288.
[21] S. Li, W.K. Liu, Reproducing kernel hierarchical partition of unity part. II: Applications, Int. J. Numer. Methods Engrg. 45 (1999) 288–317.
[22] W.K. Liu, Y. Chen, C.T. Chang, T. Belytschko, Advances in multiple scale kernel particle methods, Comput. Mech. 18 (1996) 73–111.
[23] W.K. Liu, Y. Chen, S. Jun, J.S. Chen, T. Belytschko, C. Pan, R.A. Uras, C.T. Chang, Overview and applications of the reproducing kernel methods, Arch. Comput. Methods Engrg. 3 (1996) 3–80.
[24] W.K. Liu, Y. Chen, R.A. Uras, C.T. Chang, Generalized multiple scale reproducing kernel particle methods, Comput. Methods Appl. Mech. Engrg. 139 (1996) 91–158.
[25] W.K. Liu, W. Hao, Y. Chen, S. Jun, J. Gosz, Multiresolution reproducing kernel particle methods, Comput. Mech. 20 (1997) 295–309.
[26] W.K. Liu, S. Jun, S. Zhang, Reproducing kernel particle methods, Int. J. Numer. Methods Fluids 20 (1995) 1081–1106.
[27] W.K. Liu, S. Li, T. Belytschko, Moving least square reproducing kernel method. Part I: Methodology and convergence, Comput. Methods Appl. Mech. Engrg. 143 (1997) 422–433.
[28] J.G. Malone, N.L. Johnson, A parallel finite element contact/impact algorithm for non-linear explicit transient analysis. Part II: Parallel implementation, Int. J. Numer. Methods Engrg. 37 (1994) 591–603.
[29] J.G. Malone, N.L. Johnson, A parallel finite element contact/impact algorithm for non-linear explicit transient analysis. Part I: The search algorithm and contact mechanics, Int. J. Numer. Methods Engrg. 37 (1994) 559–590.
[30] D.S. Mitrinović, Analytical Inequalities, Springer, Heidelberg, 1970.
[31] A. Needleman, Dynamic shear band development in plane strain, J. Appl. Mech. 56 (1989) 1–9.
[32] A. Needleman, Material rate dependent and mesh sensitivity in localization problems, Comput. Methods Appl. Mech. Engrg. 67 (1988) 68–85.
[33] D. Peirce, C.F. Shih, A. Needleman, A tangent modulus method for rate dependent solids, Comput. Struct. 5 (1984) 875–887.